

Article

# Prickly Pear-Like Three-Dimensional Porous MoS<sub>2</sub>: Synthesis, Characterization and Advanced Hydrogen Evolution Reaction

Huiting Lu <sup>1</sup>, Xin Chen <sup>2,\*</sup>, Wenhao Dai <sup>2</sup>, Kai Zhang <sup>2</sup>, Conghui Liu <sup>2</sup>  and Haifeng Dong <sup>2,3,\*</sup>

<sup>1</sup> Department of Chemistry, School of Chemistry and Bioengineering, University of Science & Technology Beijing, Beijing 100083, China; huitinglu@ustb.edu.cn

<sup>2</sup> Research Center for Bioengineering and Sensing Technology, Beijing Key Laboratory for Bioengineering and Sensing Technology, School of Chemistry and Bioengineering, University of Science & Technology Beijing, Beijing 100083, China; daiwenhao734028@126.com (W.D.); zzhangkai@sina.com (K.Z.); conghuilu@yeah.net (C.L.)

<sup>3</sup> Hubei Key Laboratory of Pollutant Analysis & Reuse Technology, Hubei Normal University, Huangshi 435002, China

\* Correspondence: chenxin513533@126.com (X.C.); hfdong@ustb.edu.cn (H.D.); Tel.: +86-010-82375840 (X.C. & H.D.)

Received: 8 April 2018; Accepted: 29 May 2018; Published: 4 June 2018



**Abstract:** Herein, we hydrothermally synthesize a type of prickly pear-like three-dimensional (3D) porous MoS<sub>2</sub> (ZT-MoS<sub>2</sub>), using a zinc oxide (ZnO) rod deposited on quartz glass substrates, as a template for an advanced hydrogen evolution reaction (HER) catalyst. Microscopic and spectroscopic tools comprehensively characterize the morphology of the ZT-MoS<sub>2</sub> nanostructure, which exhibits adequate edge active sites and defects, as well as a high component of active octahedral MoS<sub>2</sub> (1T-MoS<sub>2</sub>). Electrochemical characterizations reveal the good HER performance of the ZT-MoS<sub>2</sub> that presents a good overpotential of 110 mV, and a Tafel slope of 63 mV-dec<sup>-1</sup>, superior to most of the previously reported MoS<sub>2</sub>-based HER catalysts. This work contributes to the design and fabrication of 3D MoS<sub>2</sub> with enhanced HER performance, which holds great promise for fuel cells and energy conversion.

**Keywords:** three-dimensional MoS<sub>2</sub>; ZnO template; hydrogen evolution reaction; hydrothermal synthesis

## 1. Introduction

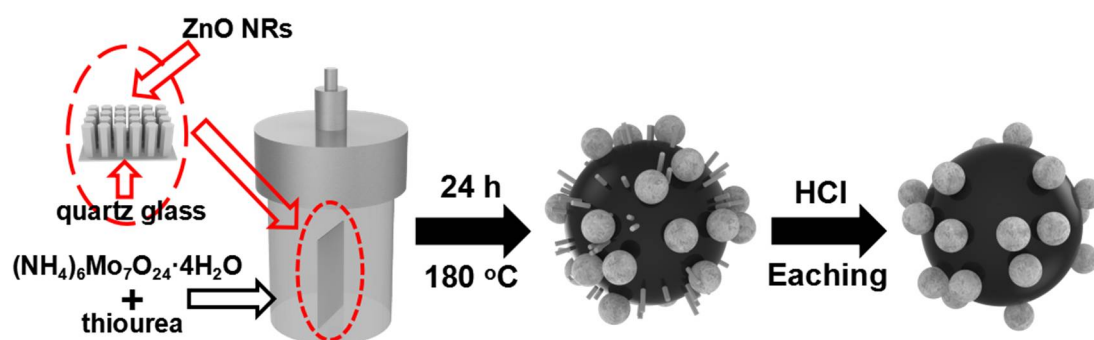
Nowadays, as an environmentally-friendly and abundant energy carrier, hydrogen is attracting intense interest for sustainable energy resources due to the energy crisis [1]. Hydrogen evolution from water splitting is the main strategy to generate hydrogen, and platinum (Pt)-based catalysts are generally employed to enhance hydrogen evolution reaction (HER) [2–5]. However, their high-cost, insufficient reservoir, and instability limit the widespread application of Pt-based catalysts. Thus, it is urgent to exploit efficient alternative catalysts, such as various transition metals and their derivatives, as well as metal-free catalysts [6–8]. Two-dimensional (2D) materials with a large specific surface area, good charge migration rate, controllable electronic properties, good stackability, and mechanical flexibility provide a unique advantage to HER catalytic activity [9]. Molybdenum sulfide (MoS<sub>2</sub>), a type of two-dimensional layered material, has attracted much attention for its unique physical and chemical properties [10]. Increasing theoretical and experimental evidence reveals that the hydrogen adsorption energy on the edge of naturally van der Waals layered MoS<sub>2</sub> is calculated to be close to that of Pt, so that MoS<sub>2</sub> has been considered as a promising substitute for Pt-based catalysts [11–13]. The edge sites of MoS<sub>2</sub> were responsible for hydrogen evolution catalytic activity, and it possessed

a lateral dimension size-dependent pattern. The deficiencies of aggregation and low conductivity of bulk MoS<sub>2</sub> limit its HER catalytic activity and widespread application [14,15].

Various efficient MoS<sub>2</sub> nanostructures with numerous active sites and good conductivity are continuously being explored. Firstly, this is an efficient strategy that introduces active edge sites into MoS<sub>2</sub>; for example, MoS<sub>2</sub> nanoplates [16], MoS<sub>2</sub> nanoparticles [17], MoS<sub>2</sub> quantum dots [18], and three dimensional (3D) MoS<sub>2</sub> [19] with numerous edge sites were developed. Secondly, MoS<sub>2</sub> nanostructures can be doped with conductive elements or deposited on highly conductive matrices to improve their conductivity. For example, Se-doped MoS<sub>2</sub> and Au-doped MoS<sub>2</sub> were designed [20,21]; MoS<sub>2</sub> nanoparticles were conjugated on carbon nanotubes [22] and graphene [23], to form MoS<sub>2</sub>-based heterogeneous composites. Moreover, this method offers a new avenue to improving the catalytic ability that fabricates MoS<sub>2</sub> with an adequate octahedral MoS<sub>2</sub> (1T-MoS<sub>2</sub>) component [24].

Among these, a 3D MoS<sub>2</sub> nanostructure with both considerable active sites and good substrate transfer ability has received intense attention. To synthesize 3D MoS<sub>2</sub>, efficient templates are a prerequisite to control the growth of MoS<sub>2</sub>. Recently, zinc oxide (ZnO) is emerging as an attractive template for constructing 3D materials, since it can be easily and controllably synthesized to produce the desired morphological structures. Various complicated nanostructures, such as silica, gold, and carbon nanotubes, using a ZnO nanostructure as a template have been reported [25–28].

Herein, using ZnO as a template, a prickly pear-like 3D porous MoS<sub>2</sub> (ZT-MoS<sub>2</sub>) was synthesized by a facile hydrothermal synthesis route (Scheme 1). The MoS<sub>2</sub> nanostructures were hydrothermally synthesized in the presence of the ZnO template deposited on the quartz glass substrate. Numerous small MoS<sub>2</sub> nanoparticles and ZnO NRs modified on the surface of big MoS<sub>2</sub> microbeads. The removal of the ZnO from the nanocomposites generated the prickly pear-like 3D ZT-MoS<sub>2</sub> nanostructure. The synthesized ZT-MoS<sub>2</sub> exhibited an outstanding HER performance with a good overpotential of 110 mV, and a small Tafel slope of 63 mV·dec<sup>-1</sup>, as well as extraordinary stability. It was superior to pure MoS<sub>2</sub> without using ZnO as template (P-MoS<sub>2</sub>), and to most previously reported MoS<sub>2</sub>-based HER catalysts.



Scheme 1. Schematic illustration of the synthesis procedure for the ZT-MoS<sub>2</sub>.

## 2. Results and Discussion

SEM, TEM, and high-resolution TEM (HRTEM) measurements (Figure 1) characterized the morphologies of the P-MoS<sub>2</sub> and ZT-MoS<sub>2</sub>. The ZT-MoS<sub>2</sub> presented a prickly pear-like structure, with numerous small MoS<sub>2</sub> nanoparticles assembled on the surface of a 2.5 μm porous MoS<sub>2</sub> microbead (Figure 1a). The pore size of the porous microbeads in the ZT-MoS<sub>2</sub> was about 135 nm (inset in Figure 1a), which was similar to the diameter of the ZnO template (Figure S1). The S-to-Mo ratio was about 2:1 (Figure S2), indicating the successful synthesis of MoS<sub>2</sub>. Zhang et al. reported that possible intergrowth would be generated between ZnO and MoS<sub>2</sub> [29]. However, the Energy Dispersive X-ray Spectrometer (EDS) analysis (Figure S2) showed there was no Zn element, which might be caused by the different synthesis processes. It was found that the ZnO template significantly affected the morphology of ZT-MoS<sub>2</sub> (Figure S3), and the HCl-mediated etching process could effectively

remove the ZnO from the ZnO-MoS<sub>2</sub> nanostructure (Figure 1a, Figures S2 and S4). The P-MoS<sub>2</sub> was a nanoflower structure with rippled and corrugated leaf structures (Figure 1d). The size of surface MoS<sub>2</sub> nanoparticles decorated on the porous MoS<sub>2</sub> microbeads in ZT-MoS<sub>2</sub> was about 350 nm (Figure 1b) (with an average surface area of  $462.1 \pm 5.2 \text{ m}^2 \text{ g}^{-1}$ , Table S1), which was smaller than that of P-MoS<sub>2</sub> (450 nm) (Figure 1e). It indicated that the ZnO controllably confines the growth of the surface MoS<sub>2</sub> nanoparticles. Both the ZT-MoS<sub>2</sub> (Figure 1c) and P-MoS<sub>2</sub> (Figure 1f) exhibited an interplanar spacing of 6.3 Å assigned to the d spacing of (002) planes of MoS<sub>2</sub>, suggesting that the ZnO did not influence the component of MoS<sub>2</sub> [30]. Compared to the smooth and regular lattice of the P-MoS<sub>2</sub>, ZT-MoS<sub>2</sub> had more delaminated MoS<sub>2</sub> (inset in Figure 1c). The resulting defects were beneficial to HER performance.

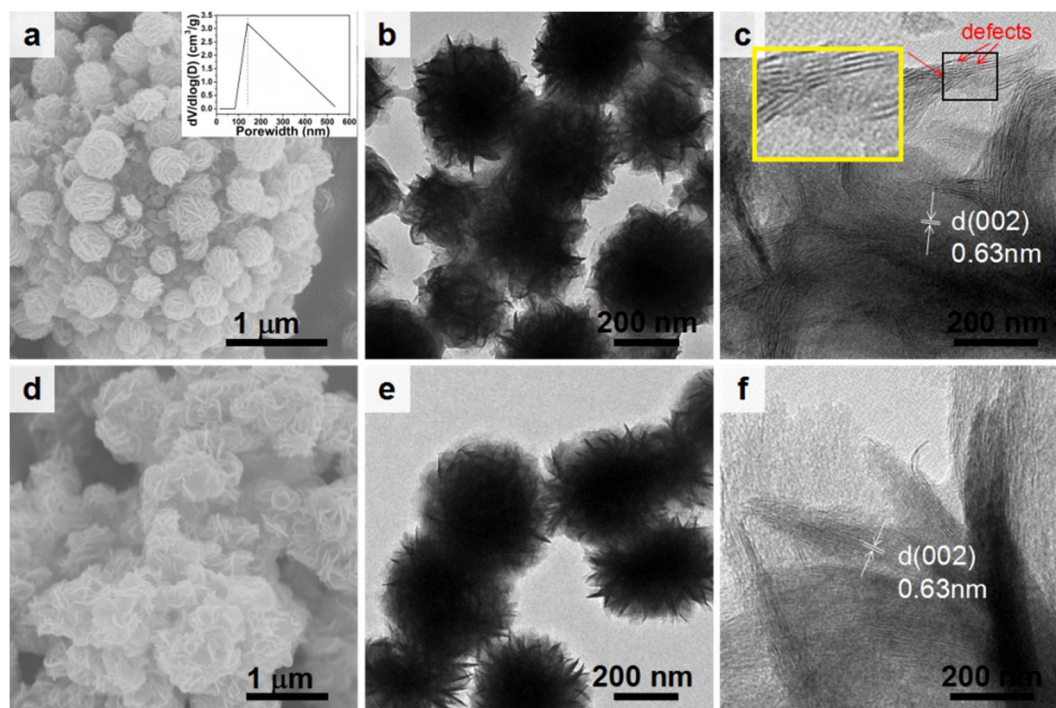


**Figure 1.** Scanning electron microscopy (SEM) images of (a) ZT-MoS<sub>2</sub> and (d) P-MoS<sub>2</sub>; transmission electron microscopy (TEM) images of (b) ZT-MoS<sub>2</sub> and (e) P-MoS<sub>2</sub>; high-resolution TEM (HRTEM) images of (c) ZT-MoS<sub>2</sub> and (f) P-MoS<sub>2</sub>. Inset a: porous size analysis of ZT-MoS<sub>2</sub>.

The composition and phase of the ZT-MoS<sub>2</sub> and P-MoS<sub>2</sub> were investigated by Raman spectroscopy analysis. ZT-MoS<sub>2</sub> presented two obvious characteristic peaks at 378 and 404 cm<sup>-1</sup>, attributed to in-plane vibration E<sub>12g</sub> modes and out-of-plane vibration A<sub>1g</sub> modes, respectively (red curve in Figure 2a) [31,32]. The characteristic peaks at 284, 490, and 234 cm<sup>-1</sup> assigned to the E<sub>1g</sub> mode forbidden in a back-scattering geometry on the surface perpendicular to the c-axis, two longitudinal acoustic (2LAM) modes, and structural-defect-induced scattering (red curve in Figure 2a) were also observed [33]. The P-MoS<sub>2</sub> exhibited similar characteristic peaks (black curve in Figure 2a) compared to the ZT-MoS<sub>2</sub>. However, the ZT-MoS<sub>2</sub> revealed a larger E<sub>12g</sub>/A<sub>1g</sub> ratio and a wider half-wavelength of E<sub>12g</sub> and A<sub>1g</sub> peaks than that of the P-MoS<sub>2</sub> (Figure 2b), which indicated that more edge structures existed in ZT-MoS<sub>2</sub> nanostructures [29]. Additionally, ZT-MoS<sub>2</sub> showed a red shift of E<sub>12g</sub> and a blue shift of A<sub>1g</sub> compared to that of P-MoS<sub>2</sub>, illustrating the thinner layered structure of ZT-MoS<sub>2</sub> when compared with P-MoS<sub>2</sub>. It could be anticipated that both the larger edge structure and thinner layered structure would lead to more active sites and endow ZT-MoS<sub>2</sub> with better HER performance than P-MoS<sub>2</sub> [34,35].

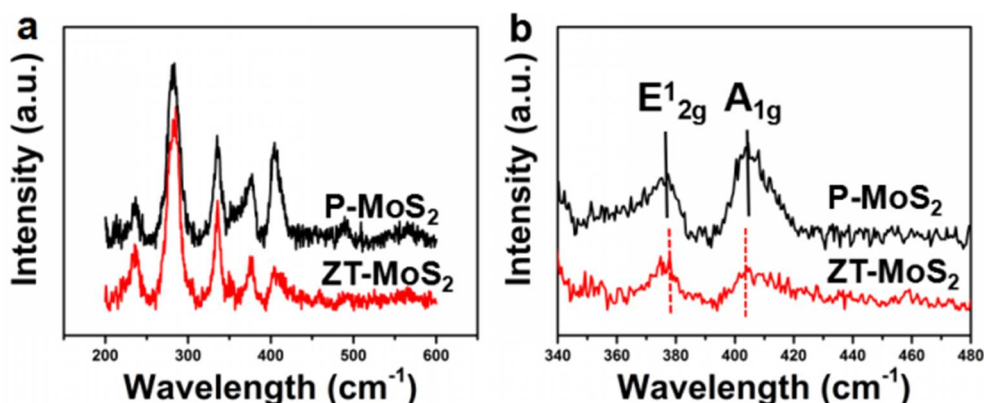


**Figure 2.** (a) Raman spectra of the P-MoS<sub>2</sub> and ZT-MoS<sub>2</sub> after HCl etching, (b) the corresponding high resolution of E<sup>1</sup><sub>2g</sub> and A<sub>1g</sub> in (a).

The high-resolution XPS of the Mo 3d peak and the corresponding S 2p peak of the ZT-MoS<sub>2</sub> and P-MoS<sub>2</sub> were depicted in Figure 3. The Mo 3d of ZT-MoS<sub>2</sub> shown in Figure 3a could be deconvoluted into four peaks of 228.9, 230.1, 232.1, and 233.6 eV assigned to Mo<sup>4+</sup> 3d<sub>5/2</sub>, Mo<sup>5+</sup> 3d<sub>5/2</sub>, Mo<sup>4+</sup> 3d<sub>3/2</sub>, and Mo<sup>5+</sup> 3d<sub>3/2</sub>, respectively. The peak of 226.2 eV ascribed to S<sup>2-</sup> 2s was also observed. Mo<sup>4+</sup> 3d<sub>5/2</sub> and Mo<sup>4+</sup> 3d<sub>3/2</sub> are related to trigonal prismatic MoS<sub>2</sub> (2H-MoS<sub>2</sub>), while Mo<sup>5+</sup> 3d<sub>5/2</sub> and Mo<sup>5+</sup> 3d<sub>3/2</sub> are associated with the 1T-MoS<sub>2</sub> [36,37]. These results illustrated the co-existence of 2H-MoS<sub>2</sub> and 1T-MoS<sub>2</sub> in the synthesized ZT-MoS<sub>2</sub>. The high-resolution XPS of S 2p presented characteristic peaks at S<sup>2-</sup> 2p<sub>3/2</sub> and S<sup>2-</sup> 2p<sub>1/2</sub> associated with 2H-MoS<sub>2</sub> at 161.6 and 162.9 eV, while S<sup>2-</sup> 2p<sub>3/2</sub> and S<sup>2-</sup> 2p<sub>1/2</sub> related to 1T-MoS<sub>2</sub> at 162.5 and 164.1 eV (Figure 3b), which further confirmed the co-existence of 1T-MoS<sub>2</sub> and 2H-MoS<sub>2</sub> in ZT-MoS<sub>2</sub> [38]. The P-MoS<sub>2</sub> exhibited higher peaks of Mo<sup>4+</sup> 3d<sub>5/2</sub> and Mo<sup>4+</sup> 3d<sub>3/2</sub> related to 2H-MoS<sub>2</sub> than the ZT-MoS<sub>2</sub> (Figure 3c), and the characteristic peaks of S<sup>2-</sup> 2p<sub>3/2</sub> and S<sup>2-</sup> 2p<sub>1/2</sub> assigned to 2H-MoS<sub>2</sub> at 161.6 and 162.9 eV were also larger than that of ZT-MoS<sub>2</sub> (Figure 3d). It was calculated that ZT-MoS<sub>2</sub> consisted of 60.7 ± 5.2% 2H-MoS<sub>2</sub> and 39.3 ± 4.3% 1T-MoS<sub>2</sub>, while P-MoS<sub>2</sub> was composed of 70.5 ± 3.8% 2H-MoS<sub>2</sub> and 29.5 ± 4.7% 1T-MoS<sub>2</sub>. The high 1T-MoS<sub>2</sub> in ZT-MoS<sub>2</sub> can also contribute to the advanced HER catalytic activity [39].

As shown in Figure 4a, the onset overpotential of ZT-MoS<sub>2</sub> was 110 ± 5 mV, which was smaller than that of P-MoS<sub>2</sub> (200 ± 4 mV) and ZnO-MoS<sub>2</sub> (240 ± 4 mV). The onset overpotential of ZT-MoS<sub>2</sub> also competed with previously reported MoS<sub>2</sub>-based HER catalysts [29,40]. The potential of the current density reached to 10 mA·cm<sup>-2</sup> was further analyzed. The potential of ZT-MoS<sub>2</sub> was 250 mV when the current density reached 10 mA·cm<sup>-2</sup>, which was smaller than the 370 and 435 mV of P-MoS<sub>2</sub> and ZnO-MoS<sub>2</sub>. The Tafel slope of the Pt/C shown in Figure 4b was 35 mV·dec<sup>-1</sup>, consistent with previous reports [20,23]. ZT-MoS<sub>2</sub> exhibited a Tafel slope of 63 mV·dec<sup>-1</sup>, smaller than the 98 mV·dec<sup>-1</sup> of P-MoS<sub>2</sub> and 107 mV·dec<sup>-1</sup> of ZnO-MoS<sub>2</sub>, suggesting that the HER reaction rate of ZnO-MoS<sub>2</sub> would increase faster along with the increase of the overpotential when compared with P-MoS<sub>2</sub> and ZnO-MoS<sub>2</sub> [41]. The electrochemical impedance spectroscopy (EIS) measurements (Figure 4c) revealed a smaller impedance of the ZT-MoS<sub>2</sub> than the P-MoS<sub>2</sub>. It demonstrated that ZT-MoS<sub>2</sub> dramatically enhanced the electron transfer and reaction mass accessibility to the active sites. Furthermore, we carried out a long-term cycling test for more than 5000 cycles to investigate the stability of ZT-MoS<sub>2</sub>. The negligible difference before and after 5000 cycles indicated the remarkable stability of ZT-MoS<sub>2</sub> during the long-term electrochemical catalytic process (Figure 4d). The turnover frequency (TOF) for the active sites of the ZT-MoS<sub>2</sub> catalyst was calculated using the roughness factor method according to the following equation [42]. The ZT-MoS<sub>2</sub> presented a TOF of 1.25 s<sup>-1</sup>. It was 1.81-fold higher than the TOF of P-MoS<sub>2</sub> (0.69 s<sup>-1</sup>), further indicating the advanced HER catalytic activity of ZT-MoS<sub>2</sub> (Figure S5).

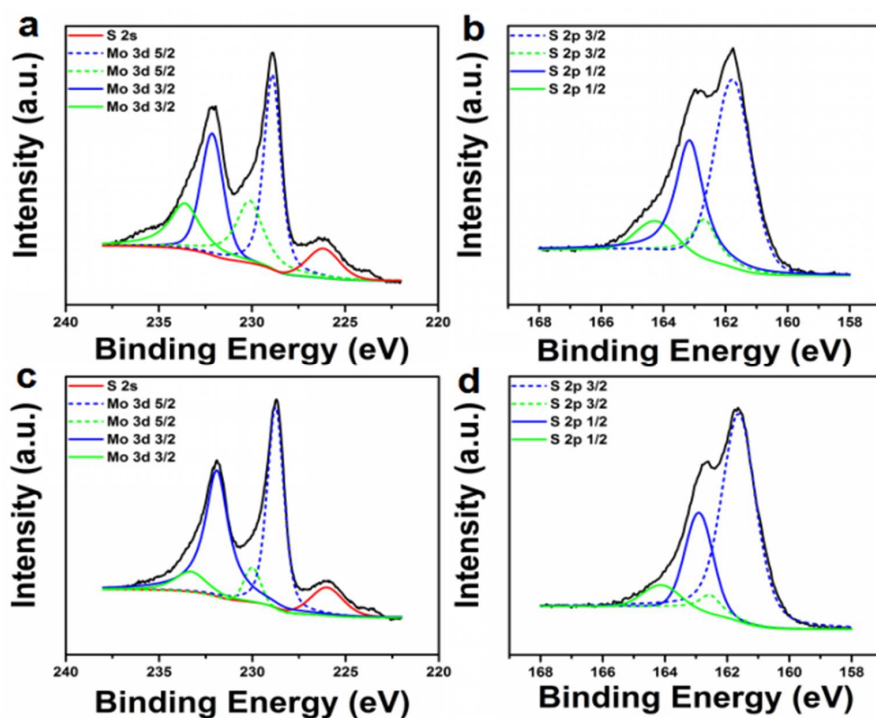


**Figure 3.** High resolution X-ray photoelectron spectroscopy (XPS) spectrum recorded for the Mo 3d of (a) ZT-MoS<sub>2</sub> and (c) P-MoS<sub>2</sub>, and S 2p of (b) ZT-MoS<sub>2</sub> (d) P-MoS<sub>2</sub>. The data were the average of three measurements.

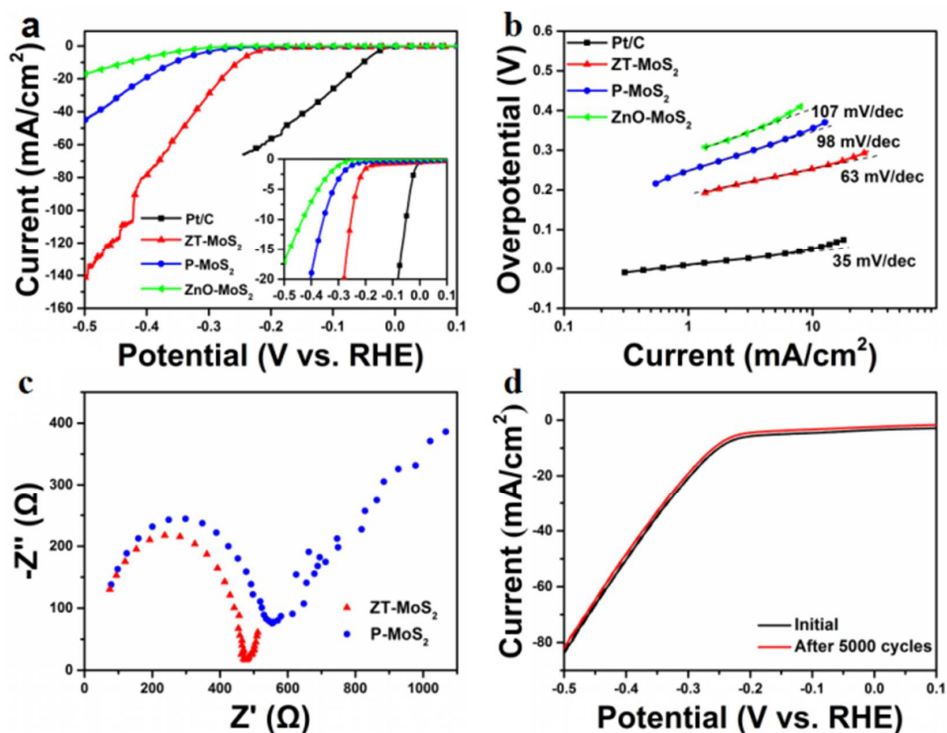


**Figure 4.** Electrochemical characterizations of as-product catalysts. (a) Polarization curves of Pt/C, ZT-MoS<sub>2</sub>, P-MoS<sub>2</sub>, ZnO-MoS<sub>2</sub>. (b) Tafel plots of Pt/C, ZT-MoS<sub>2</sub>, P-MoS<sub>2</sub>, ZnO-MoS<sub>2</sub>. (c) Electrochemical impedance spectroscopy (EIS) Nyquist plots of ZT-MoS<sub>2</sub> and P-MoS<sub>2</sub>. (d) Durability test of ZT-MoS<sub>2</sub> through 5000 cycles linear sweep voltammetry (LSV).

These results revealed the superb HER catalytic ability of ZT-MoS<sub>2</sub>, which can be explained as follows: firstly, the unique prickly pear-like 3D porous MoS<sub>2</sub> structures possess many edge active sites confirmed by HRTEM (Figure 1e) and Raman Spectrum analysis (Figure 2b), which contribute to the advanced HER performance (Figure 4a,b). Moreover, adequate defects (Figure 1e) and abundant 1T-MoS<sub>2</sub> (Figure 3a,b) were included in ZT-MoS<sub>2</sub>, enabling the advanced HER catalytic activity. Lastly, the porous 3D structure facilitated the reaction mass transfer during the reaction, which creates the ready accessibility of active sites to the substrate, while the surface of the nanostructure also contributed to its good performance (Table S1). In comparison, both the MoS<sub>2</sub> microbeads without decorated MoS<sub>2</sub> nanoparticles and the MoS<sub>2</sub> microbeads decorated with crowded MoS<sub>2</sub> nanoparticles (Figure S3) exhibited inferior HER to ZT-MoS<sub>2</sub> (Figure S6). The negligible difference before and after a 5000 cycles long-term test (Figure 4d) indicated the extraordinary stability of the synthesized ZT-MoS<sub>2</sub>. It suggested that the numerous edge active sites and the good accessibility of active sites to the reaction substrate were significant factors in the efficient HER performance.

### 3. Materials and Methods

#### 3.1. Reagent

Zinc nitrate hexahydrate (Zn(NO<sub>3</sub>)<sub>2</sub>·6H<sub>2</sub>O), hexamethylenetetramine (C<sub>6</sub>H<sub>12</sub>N<sub>4</sub>), zinc acetate dihydrate (C<sub>4</sub>H<sub>10</sub>O<sub>6</sub>Zn), thiourea (H<sub>2</sub>NCSN<sub>2</sub>), and hexaammonium heptamolybdate tetrahydrate ((NH<sub>4</sub>)<sub>6</sub>Mo<sub>7</sub>O<sub>24</sub>·4H<sub>2</sub>O) were purchased from Sigma (St. Louis, MO, USA). Potassium hexacyanoferrate (III) (K<sub>3</sub>Fe(CN)<sub>6</sub>), potassium hexacyanoferrate (II) trihydrate (K<sub>4</sub>Fe(CN)<sub>6</sub>·3H<sub>2</sub>O), potassium chloride (KCl), hydrochloric acid (HCl), sulfuric acid (H<sub>2</sub>SO<sub>4</sub>), and ethanol absolute were purchased from Sinopharm Chemical Reagent Co., Ltd. (Shanghai, China). All reagents used in this study were of analytical grade.

#### 3.2. Preparation of ZnO Nanorods (NRs)

The ZnO NRs were synthesized in accordance with a method set out in a previous report, with some modification [43]. Briefly, ZnO NRs were synthesized on quartz glass substrates with dimensions of 5.5 × 2.5 cm. Firstly, a droplet of 2 mL zinc acetate (5 mM) in ethanol was spin-coated on the quartz glass substrates three times, and then the quartz glass was annealed at 300 °C for 30 min in a tube furnace. The resulting quartz glass was kept in the aqueous solution containing zinc nitrate hexahydrate (50 mM) and hexamethylenetetramine (50 mM) at 100 °C for 10 h in a sealed Schott-Duran bottle. Following this, the substrates were then rinsed thoroughly with ultrapure water and dried overnight at 60 °C in an oven.

#### 3.3. Fabrication of ZT-MoS<sub>2</sub> and P-MoS<sub>2</sub>

(NH<sub>4</sub>)<sub>6</sub>Mo<sub>7</sub>O<sub>24</sub>·4H<sub>2</sub>O (1 mmol) and thiourea (30 mmol) were dissolved in ultrapure water (40 mL) to form a homogeneous solution, and the solution was transferred to a 50 mL Teflon-lined stainless-steel autoclave. Different amounts of prepared quartz glass (0.5, 1, and 2) were immersed into the Teflon-lined stainless-steel autoclave and kept at 180 °C for 24 h to obtain different ZT-MoS<sub>2</sub> (termed as ZT-MoS<sub>2</sub>-H, ZT-MoS<sub>2</sub> and ZT-MoS<sub>2</sub>-T, respectively). The solution was naturally cooled down to room temperature, and 3 mL 10% HCl solution was added to etch the ZnO NRs. The resulting ZT-MoS<sub>2</sub> dispersed in the solution was generated by centrifuging at 8000 rpm, which was washed thoroughly in the ultrapure water, and then dried at 60 °C by a vacuum freeze dryer to obtain about 4 mg ZT-MoS<sub>2</sub> powder each time.

(NH<sub>4</sub>)<sub>6</sub>Mo<sub>7</sub>O<sub>24</sub>·4H<sub>2</sub>O (1 mmol) and thiourea (30 mmol) were dissolved in ultrapure water (40 mL) to form a homogeneous solution and the solution was transferred to a 50 mL Teflon-lined stainless-steel autoclave. The solution was naturally cooled down to room temperature and 3 mL HCl solution was added. The resulting P-MoS<sub>2</sub> dispersed in the solution was generated by centrifuging at 8000 rpm,

which was washed thoroughly in the ultrapure water, and then dried at 60 °C by a vacuum freeze dryer to obtain P-MoS<sub>2</sub> powder.

### 3.4. Characterization

The morphologies of these products were observed under scanning electron microscopy (SEM) (HITACHI S-4800, Tokyo, Japan) and transmission electron microscopy (TEM) (JEM-2010, JEOL Ltd., Tokyo, Japan, 200 kV). High-resolution TEM images were taken using a JEOL 2100F microscope (JEOL Ltd., Tokyo, Japan, 200 kV) with an accelerating voltage of 200 kV. X-ray photoelectron spectroscopy (XPS) measurements were performed using an AXIS ULTRADLD instrument (Kratos, Manchester, UK) equipped with an Al K $\alpha$  X-ray source. Raman spectra were recorded on an InVia-Reflex Raman microscope (Renishaw, London, UK) with a laser excitation wavelength of 532 nm. The porosity was performed with a nitrogen adsorption–desorption isotherm using a surface area analyzer (QuadraSorb SI 2000-08, Quantachrome Instruments, Boynton Beach, FL, USA).

### 3.5. Electrochemical Measurements

Electrochemical measurements were performed using an electrochemical station (CHI 852C, Shanghai Chenhua Instrument Co., Shanghai, China) in a three-electrode system. A three-electrode system was employed, consisting of a saturated calomel electrode (SCE) as the reference electrode, a graphite rod as the counter electrode, and a glassy carbon rotating disk electrode (RDE) or glassy carbon electrode (GCE) loaded on the catalyst as the working electrode. Linear sweep voltammetry (LSV) measurements were run in 0.5 M H<sub>2</sub>SO<sub>4</sub> (purged with pure N<sub>2</sub>) at a scan rate of 5 mV·s<sup>-1</sup> and at 1400 rpm [17]. For durability measurement, the LSV was performed at a scan rate of 50 mV·s<sup>-1</sup> from 0.2 to -0.6 V for 5000 cycles.

Typically, 2 mg of the catalyst was dispersed in 2 mL of ultrapure water to form homogeneous ink under sonication. Then, 20  $\mu$ L of the catalyst ink was loaded onto the RDE (3 mm in diameter, loading  $\sim$ 0.283 mg·cm<sup>-2</sup>). 5  $\mu$ L of 1 wt % Nafion solution was dropped onto the electrode after the ink was dried. Cyclic Voltammetry (CV) measurements using GCE as the working electrode were run in 0.5 M H<sub>2</sub>SO<sub>4</sub> (purged with pure N<sub>2</sub>) at scan rates of 150, 120, 90, 60, 30, and 10 mV·s<sup>-1</sup>, respectively. The EIS measurements were recorded in the same configuration using the 1 mmol·L<sup>-1</sup> K<sub>3</sub>Fe(CN)<sub>6</sub>, 1 mmol·L<sup>-1</sup> K<sub>4</sub>Fe(CN)<sub>6</sub>·3H<sub>2</sub>O, 0.1 mol·L<sup>-1</sup> KCl as the electrolyte at  $\eta = 0.2$  V from 10<sup>-2</sup> to 5  $\times$  10<sup>5</sup> Hz with a voltage amplitude of 5 mV.

## 4. Conclusions

In conclusion, a prickly pear-like 3D porous MoS<sub>2</sub> nanostructure with advanced HER performance was developed by using a simple and ZnO-mediated hydrothermal synthesis route. Comprehensive microscopic and spectroscopic measurements including SEM, TEM, HRTEM, Raman spectra, and XPS were employed to characterize the morphology and components of the ZT-MoS<sub>2</sub>. The prickly pear-like 3D porous ZT-MoS<sub>2</sub> consisted of numerous small MoS<sub>2</sub> nanoparticles decorated on large porous MoS<sub>2</sub> microbeads. It displayed many edge active sites and defects as well as abundant 1T-MoS<sub>2</sub>. The ZT-MoS<sub>2</sub> exhibited a superior HER catalytic activity compared with structures using P-MoS<sub>2</sub> as a template, and most of the previously reported MoS<sub>2</sub>-based HER catalysts, such as MoS<sub>2</sub>/MoSe<sub>2</sub> films [31] and Core-shell MoO<sub>3</sub>-MoS<sub>2</sub> nanowires [41]. Additionally, ZT-MoS<sub>2</sub> presented extraordinary stability during the long-term cycling test. This work paves a new avenue for the controllable design of efficient 3D MoS<sub>2</sub> with advanced HER performance, which can be easily extended to other analogous materials.

**Supplementary Materials:** The following are available online at <http://www.mdpi.com/2073-4344/8/6/235/s1>, Table S1: HER activities of synthesized MoS<sub>2</sub> catalysts, Figure S1: (a) SEM image and (b) corresponding magnified SEM image of ZnO NRs, Figure S2: Energy Dispersive X-ray Spectrometer (EDS) spectrum of ZT-MoS<sub>2</sub>, Figure S3: SEM image of different ZT-MoS<sub>2</sub>: (a) ZT-MoS<sub>2</sub>-H, (b) ZT-MoS<sub>2</sub> and (c) ZT-MoS<sub>2</sub>-T, Figure S4: SEM image of MoS<sub>2</sub> before HCl etching, Figure S5: Electrochemical measurement for determining TOF: (a) a cyclic voltammetry (CV) curve of ZT-MoS<sub>2</sub> at different scan rates. (b) Current density of CV experiment at overpotential 500 mV vs. RHE

as a function of scan rates, Figure S6: Polarization curves of different ZT-MoS<sub>2</sub>: (a) ZT-MoS<sub>2</sub>-H, (b) ZT-MoS<sub>2</sub> and (c) ZT-MoS<sub>2</sub>-T.

**Author Contributions:** H.D. and X.C. conceived the project. H.L. designed the experiment and synthesized the material; W.D. and K.Z. carried out the characterization of materials; X.C. and C.L. performed the electrochemical Measurements; H.L. and X.C. analyzed the data and wrote the main manuscript text; H.D. modified the manuscript. All authors have given approval to the final version of the manuscript.

**Acknowledgments:** The work was supported by National Key R&D Program of China (Grant Nos. 2016YFC0106602 and 2016YFC0106601); National Natural Science Foundation of China (Grant Nos. 21645005, 21475008); the Open Research Fund Program of Beijing Key Lab of Plant Resource Research and Development, Beijing Technology and Business University (PRRD-2016-YB2); the Open Research Fund Program of Hubei Key Laboratory of Pollutant Analysis & Reuse Technology, Hubei Normal University (PA160105).

**Conflicts of Interest:** The authors declare no conflicts of interest.

## References

1. Dresselhaus, M.S.; Thomas, I.L. Alternative energy technologies. *Nature* **2001**, *414*, 332–337. [[CrossRef](#)] [[PubMed](#)]
2. Bard, A.J.; Fox, M.A. Artificial photosynthesis: Solar splitting of water to hydrogen and oxygen. *Acc. Chem. Res.* **1995**, *28*, 141–145. [[CrossRef](#)]
3. Walter, M.G.; Warren, E.L.; McKone, J.R.; Boettcher, S.W.; Mi, Q.X.; Santori, E.A.; Lewis, N.S. Solar water splitting cells. *Chem. Rev.* **2010**, *110*, 6446–6473. [[CrossRef](#)] [[PubMed](#)]
4. Norskov, J.K.; Christensen, C.H. Chemistry—Toward efficient hydrogen production at surfaces. *Science* **2006**, *312*, 1322–1323. [[CrossRef](#)] [[PubMed](#)]
5. Greeley, J.; Jaramillo, T.F.; Bonde, J.; Chorkendorff, I.B.; Norskov, J.K. Computational high-throughput screening of electrocatalytic materials for hydrogen evolution. *Nat. Mater.* **2006**, *5*, 909–913. [[CrossRef](#)] [[PubMed](#)]
6. Hou, Y.D.; Laursen, A.B.; Zhang, J.S.; Zhang, G.G.; Zhu, Y.S.; Wang, X.C.; Dahl, S.; Chorkendorff, I. Layered nanojunctions for hydrogen-evolution catalysis. *Angew. Chem. Int. Ed.* **2013**, *52*, 3621–3625. [[CrossRef](#)] [[PubMed](#)]
7. Li, Y.G.; Hasin, P.; Wu, Y.Y. Ni<sub>x</sub>CO<sub>3</sub>-XO<sub>4</sub> nanowire arrays for electrocatalytic oxygen evolution. *Adv. Mater.* **2010**, *22*. [[CrossRef](#)] [[PubMed](#)]
8. Casado-Rivera, E.; Volpe, D.J.; Alden, L.; Lind, C.; Downie, C.; Vazquez-Alvarez, T.; Angelo, A.C.D.; DiSalvo, F.J.; Abruna, H.D. Electrocatalytic activity of ordered intermetallic phases for fuel cell applications. *J. Am. Chem. Soc.* **2004**, *126*, 4043–4049. [[CrossRef](#)] [[PubMed](#)]
9. Di, J.; Yan, C.; Handoko, A.D.; Seh, Z.W.; Li, H.; Liu, Z. Ultrathin two-dimensional materials for photo- and electrocatalytic hydrogen evolution. *Mater. Today* **2018**. [[CrossRef](#)]
10. Benck, J.D.; Hellstern, T.R.; Kibsgaard, J.; Chakthranont, P.; Jaramillo, T.F. Catalyzing the hydrogen evolution reaction (HER) with molybdenum sulfide nanomaterials. *ACS Catal.* **2014**, *4*, 3957–3971. [[CrossRef](#)]
11. Karunadasa, H.I.; Montalvo, E.; Sun, Y.J.; Majda, M.; Long, J.R.; Chang, C.J. A molecular MoS<sub>2</sub> edge site mimic for catalytic hydrogen generation. *Science* **2012**, *335*, 698–702. [[CrossRef](#)] [[PubMed](#)]
12. Laursen, A.B.; Kegnaes, S.; Dahl, S.; Chorkendorff, I. Molybdenum sulfides-efficient and viable materials for electro- and photoelectrocatalytic hydrogen evolution. *Energy Environ. Sci.* **2012**, *5*, 5577–5591. [[CrossRef](#)]
13. Wang, T.Y.; Liu, L.; Zhu, Z.W.; Papakonstantinou, P.; Hu, J.B.; Liu, H.Y.; Li, M.X. Enhanced electrocatalytic activity for hydrogen evolution reaction from self-assembled monodispersed molybdenum sulfide nanoparticles on an Au electrode. *Energy Environ. Sci.* **2013**, *6*, 625–633. [[CrossRef](#)]
14. Kibsgaard, J.; Chen, Z.B.; Reinecke, B.N.; Jaramillo, T.F. Engineering the surface structure of MoS<sub>2</sub> to preferentially expose active edge sites for electrocatalysis. *Nat. Mater.* **2012**, *11*, 963–969. [[CrossRef](#)] [[PubMed](#)]
15. Jaramillo, T.F.; Jorgensen, K.P.; Bonde, J.; Nielsen, J.H.; Horch, S.; Chorkendorff, I. Identification of active edge sites for electrochemical H<sub>2</sub> evolution from MoS<sub>2</sub> nanocatalysts. *Science* **2007**, *317*, 100–102. [[CrossRef](#)] [[PubMed](#)]
16. Yan, Y.; Xia, B.Y.; Ge, X.M.; Liu, Z.L.; Wang, J.Y.; Wang, X. Ultrathin MoS<sub>2</sub> nanoplates with rich active sites as highly efficient catalyst for hydrogen evolution. *ACS Appl. Mater. Interfaces* **2013**, *5*, 12794–12798. [[CrossRef](#)] [[PubMed](#)]

17. Dong, H.F.; Liu, C.H.; Ye, H.T.; Hu, L.P.; Fugetsu, B.S.; Dai, W.H.; Cao, Y.; Qi, X.Q.; Lu, H.T.; Zhang, X.J. Three-dimensional nitrogen-doped graphene supported molybdenum disulfide nanoparticles as an advanced catalyst for hydrogen evolution reaction. *Sci. Rep.* **2015**, *5*, 17542. [[CrossRef](#)] [[PubMed](#)]
18. Xu, S.J.; Li, D.; Wu, P.Y. One-pot, facile, and versatile synthesis of monolayer MoS<sub>2</sub>/WS<sub>2</sub> quantum dots as bioimaging probes and efficient electrocatalysts for hydrogen evolution reaction. *Adv. Funct. Mater.* **2015**, *25*, 1127–1136. [[CrossRef](#)]
19. Zhou, W.J.; Zhou, K.; Hou, D.M.; Liu, X.J.; Li, G.Q.; Sang, Y.H.; Liu, H.; Li, L.G.; Chen, S.W. Three-dimensional hierarchical frameworks based on MoS<sub>2</sub> nanosheets self-assembled on graphene oxide for efficient electrocatalytic hydrogen evolution. *ACS Appl. Mater. Interfaces* **2014**, *6*, 21534–21540. [[CrossRef](#)] [[PubMed](#)]
20. Ren, X.P.; Ma, Q.; Fan, H.B.; Pang, L.Q.; Zhang, Y.X.; Yao, Y.; Ren, X.D.; Liu, S.Z. A Se-doped MoS<sub>2</sub> nanosheet for improved hydrogen evolution reaction. *Chem. Commun.* **2015**, *51*, 15997–16000. [[CrossRef](#)] [[PubMed](#)]
21. Shi, Y.; Wang, J.; Wang, C.; Zhai, T.T.; Bao, W.J.; Xu, J.J.; Xia, X.H.; Chen, H.Y. Hot electron of Au nanorods activates the electrocatalysis of hydrogen evolution on MoS<sub>2</sub> nanosheets. *J. Am. Chem. Soc.* **2015**, *137*, 7365–7370. [[CrossRef](#)] [[PubMed](#)]
22. Li, P.; Yang, Z.; Shen, J.X.; Nie, H.G.; Cai, Q.R.; Li, L.H.; Ge, M.Z.; Gu, C.C.; Chen, X.; Yang, K.Q.; et al. Subnanometer molybdenum sulfide on carbon nanotubes as a highly active and stable electrocatalyst for hydrogen evolution reaction. *ACS Appl. Mater. Interfaces* **2016**, *8*, 3543–3550. [[CrossRef](#)] [[PubMed](#)]
23. Li, Y.G.; Wang, H.L.; Xie, L.M.; Liang, Y.Y.; Hong, G.S.; Dai, H.J. MoS<sub>2</sub> nanoparticles grown on graphene: An advanced catalyst for the hydrogen evolution reaction. *J. Am. Chem. Soc.* **2011**, *133*, 7296–7299. [[CrossRef](#)] [[PubMed](#)]
24. Voiry, D.; Salehi, M.; Silva, R.; Fujita, T.; Chen, M.W.; Asefa, T.; Shenoy, V.B.; Eda, G.; Chhowalla, M. Conducting MoS<sub>2</sub> nanosheets as catalysts for hydrogen evolution reaction. *Nano Lett.* **2013**, *13*, 6222–6227. [[CrossRef](#)] [[PubMed](#)]
25. Krishna, K.S.; Vivekanandan, G.; Ravinder, D.; Eswaramoorthy, M. ZnO: A versatile template to obtain unusual morphologies of silica, gold and carbon nanostructures. *Chem. Commun.* **2010**, *46*, 2989–2991. [[CrossRef](#)] [[PubMed](#)]
26. Zeng, H.B.; Cai, W.P.; Liu, P.S.; Xu, X.X.; Zhou, H.J.; Klingshirn, C.; Kalt, H. ZnO-based hollow nanoparticles by selective etching: Elimination and reconstruction of metal-semiconductor interface, improvement of blue emission and photocatalysis. *ACS Nano* **2008**, *2*, 1661–1670. [[CrossRef](#)] [[PubMed](#)]
27. Gong, W.; Chen, W.S.; He, J.P.; Tong, Y.; Liu, C.; Su, L.; Gao, B.W.; Yang, H.K.; Zhang, Y.; Zhang, X.J. Substrate-independent and large-area synthesis of carbon nanotube thin films using ZnO nanorods as template and dopamine as carbon precursor. *Carbon* **2015**, *83*, 275–281. [[CrossRef](#)]
28. Liu, J.P.; Jiang, J.; Bosman, M.; Fan, H.J. Three-dimensional tubular arrays of MnO<sub>2</sub>-NiO nanoflakes with high areal pseudocapacitance. *J. Mater. Chem.* **2012**, *22*, 2419–2426. [[CrossRef](#)]
29. Zhang, K.N.; Zhang, Y.; Zhang, T.N.; Dong, W.J.; Wei, T.X.; Sun, Y.; Chen, X.; Shen, G.Z.; Dai, N. Vertically coupled ZnO nanorods on MoS<sub>2</sub> monolayers with enhanced Raman and photoluminescence emission. *Nano Res.* **2015**, *8*, 743–750. [[CrossRef](#)]
30. Kong, D.S.; Wang, H.T.; Cha, J.J.; Pasta, M.; Koski, K.J.; Yao, J.; Cui, Y. Synthesis of MoS<sub>2</sub> and MoSe<sub>2</sub> films with vertically aligned layers. *Nano Lett.* **2013**, *13*, 1341–1347. [[CrossRef](#)] [[PubMed](#)]
31. Rao, C.N.R.; Matte, H.; Maitra, U. Graphene analogues of inorganic layered materials. *Angew. Chem. Int. Ed.* **2013**, *52*, 13162–13185. [[CrossRef](#)] [[PubMed](#)]
32. Wang, H.T.; Lu, Z.Y.; Kong, D.S.; Sun, J.; Hymel, T.M.; Cui, Y. Electrochemical tuning of MoS<sub>2</sub> nanoparticles on three-dimensional substrate for efficient hydrogen evolution. *ACS Nano* **2014**, *8*, 4940–4947. [[CrossRef](#)] [[PubMed](#)]
33. Lee, C.; Yan, H.; Brus, L.E.; Heinz, T.F.; Hone, J.; Ryu, S. Anomalous lattice vibrations of single- and few-layer MoS<sub>2</sub>. *ACS Nano* **2010**, *4*, 2695–2700. [[CrossRef](#)] [[PubMed](#)]
34. Hinnemann, B.; Moses, P.G.; Bonde, J.; Jorgensen, K.P.; Nielsen, J.H.; Horch, S.; Chorkendorff, I.; Nørskov, J.K. Biornimetic hydrogen evolution: MoS<sub>2</sub> nanoparticles as catalyst for hydrogen evolution. *J. Am. Chem. Soc.* **2005**, *127*, 5308–5309. [[CrossRef](#)] [[PubMed](#)]
35. Xie, J.F.; Zhang, H.; Li, S.; Wang, R.X.; Sun, X.; Zhou, M.; Zhou, J.F.; Lou, X.W.; Xie, Y. Defect-rich MoS<sub>2</sub> ultrathin nanosheets with additional active edge sites for enhanced electrocatalytic hydrogen evolution. *Adv. Mater.* **2013**, *25*. [[CrossRef](#)] [[PubMed](#)]

36. Shi, Y.M.; Wang, Y.; Wong, J.I.; Tan, A.Y.S.; Hsu, C.L.; Li, L.J.; Lu, Y.C.; Yang, H.Y. Self-assembly of hierarchical MoS<sub>x</sub>/CNT nanocomposites (2 < x < 3): Towards high performance anode materials for lithium ion batteries. *Sci. Rep.* **2013**, *3*, 2169. [[CrossRef](#)] [[PubMed](#)]
37. Pingli, Q.; Guojia, F.; Weijun, K.; Fei, C.; Qiao, Z.; Jiawei, W.; Hongwei, L.; Xingzhong, Z. In situ growth of double-layer MoO<sub>3</sub>/MoS<sub>2</sub> film from MoS<sub>2</sub> for hole-transport layers in organic solar cell. *J. Mater. Chem. A* **2014**, *2*, 2742–2756. [[CrossRef](#)]
38. Dai, W.H.; Dong, H.F.; Fugetsu, B.; Cao, Y.; Lu, H.T.; Ma, X.L.; Zhang, X.J. Tunable fabrication of molybdenum disulfide quantum dots for intracellular microRNA detection and multiphoton bioimaging. *Small* **2015**, *11*, 4158–4164. [[CrossRef](#)] [[PubMed](#)]
39. Lukowski, M.A.; Daniel, A.S.; Meng, F.; Forticaux, A.; Li, L.S.; Jin, S. Enhanced hydrogen evolution catalysis from chemically exfoliated metallic MoS<sub>2</sub> nanosheets. *J. Am. Chem. Soc.* **2013**, *135*, 10274–10277. [[CrossRef](#)] [[PubMed](#)]
40. Chen, Z.B.; Cummins, D.; Reinecke, B.N.; Clark, E.; Sunkara, M.K.; Jaramillo, T.F. Core-shell MoO<sub>3</sub>-MoS<sub>2</sub> nanowires for hydrogen evolution: A functional design for electrocatalytic materials. *Nano Lett.* **2011**, *11*, 4168–4175. [[CrossRef](#)] [[PubMed](#)]
41. Merki, D.; Hu, X.L. Recent developments of molybdenum and tungsten sulfides as hydrogen evolution catalysts. *Energy Environ. Sci.* **2011**, *4*, 3878–3888. [[CrossRef](#)]
42. Behranginia, A.; Asadi, M.; Liu, C.; Yasaei, P.; Kumar, B.; Phillips, P.; Foroozan, T.; Waranius, J.C.; Kim, K.; Abiade, J.; et al. Highly efficient hydrogen evolution reaction using crystalline layered three-dimensional molybdenum disulfides grown on graphene film. *Chem. Mater.* **2016**, *28*, 549–555. [[CrossRef](#)]
43. Handoko, A.D.; Liew, L.-L.; Lin, M.; Sankar, G.; Du, Y.; Su, H.; Dong, Z.; Goh, G.K.L. Elucidation of thermally induced internal porosity in zinc oxide nanorods. *Nano Res.* **2018**, *11*, 2412–2423. [[CrossRef](#)]



© 2018 by the authors. Licensee MDPI, Basel, Switzerland. This article is an open access article distributed under the terms and conditions of the Creative Commons Attribution (CC BY) license (<http://creativecommons.org/licenses/by/4.0/>).